POLITECNICO DI TORINO
Repository ISTITUZIONALE

On the notch sensitivity of asbuilt Laser Beam Powder Bed–Fused AlSi10Mg specimens subjected to Very High Cycle Fatigue tests at ultrasonic frequency up to 109cycles

(Article begins on next page)

25 November 2024

SPECIAL ISSUE ARTICLE

FFEMS Fatigue & Fracture of Engineering Materials & Structures   WILEY

On the notch sensitivity of as-built Laser Beam Powder Bed–Fused AlSi10Mg specimens subjected to Very High Cycle Fatigue tests at ultrasonic frequency up to 10^9 cycles

Andrea Tridello[1] | Carlo Boursier Niutta[1] | Alessandro Benelli[2] |
Ana Paula Pagnoncelli[3] | Massimo Rossetto[1] | Filippo Berto[4] |
Davide Salvatore Paolino[1]

[1]Department of Mechanical and Aerospace Engineering, Politecnico di Torino, Turin, Italy

[2]Department of Applied Science and Technology, Politecnico di Torino, Turin, Italy

[3]Campus Management, Logistics, and Sustainability, Politecnico di Torino, Turin, Italy

[4]Department of Chemical Engineering, Materials, and Environment, Università La Sapienza, Rome, Italy

Correspondence
A. Tridello, Department of Mechanical and Aerospace Engineering, Politecnico di Torino, C.so Duca degli Abruzzi 24, Turin 10129, Italy.
Email: andrea.tridello@polito.it

Abstract

The notch effect significantly influences the fatigue response of components and is particularly relevant for parts produced with additive manufacturing (AM) processes, characterized by complex geometries and possible geometric discontinuities inducing local and critical peak stresses. Moreover, the low surface quality, as well as manufacturing defects and residual stresses, interacts with the local peak stress induced by geometric discontinuities, complicating the assessment of the notch effect for AM parts and requiring extensive experimental fatigue investigations. In the present paper, the notch sensitivity of as-built AlSi10Mg specimens produced with the laser beam powder bed fusion in the Very High Cycle Fatigue regime is investigated. Ultrasonic fatigue tests up to 10^9 cycles have been carried out on rectangular bars and rectangular bars with a central through-thickness hole. The notch effect has been found to significantly affect the fatigue response of the investigated AlSi10Mg specimens, with surface defects having a main role and pointing out the influence of the surface quality on the crack formation.

KEYWORDS
additive manufacturing, AlSi10Mg, laser beam powder bed fusion (LB-PBF), notch effect, very high cycle fatigue (VHCF)

Highlights

- Notch sensitivity on the very high cycle fatigue (VHCF) response of AlSi10Mg specimens is investigated.
- The AlSi10Mg VHCF fatigue response is strongly influenced by the notch.

- The experimental fatigue notch factor is close to that computed with literature models.
- Experimental tests are recommended to account for the large experimental scatter.

1 | INTRODUCTION

The geometry of parts used in machinery components for industrial and structural applications is characterized by geometric discontinuities, like holes, grooves, fillets, or, in general, by notches, which significantly affect their structural integrity.[1–5] The local stress increment and the stress gradient induced by discontinuities influence the performance of the component and, in particular, its response to cyclic loads. The sensitivity to notch effect depends, in general, on the geometry of the discontinuity and on the material.[1] However, the stress gradient and the local volume in which the peak stress is present also play a significant role.[6–8] Notch effect should be therefore properly evaluated during the design stage, and the research on fatigue notch and on models for predicting its effect is fundamental to ensure the structural integrity of components used in industrial applications.[2]

The issues concerning notch effects are particularly accentuated when dealing with components produced with additive manufacturing (AM) processes. Indeed, components with complex shapes and geometries, which were not producible in the past with traditional methodologies, can be currently manufactured with AM processes.[9] The design freedom ensured by AM processes permits to optimize the component topology, with topology optimization (TO) algorithms effectively employed for the design.[10–12] However, local discontinuities and localized changes of the geometry can be present in the optimized component to allow the connection of the part with the other components of the structure or for post-treatment processes.[13] With these complex geometries typical of TO parts manufactured with AM processes, notches can be critical, with the possible propagation of cracks eventually leading to a premature failure even for low-amplitude loads. Furthermore, the complex stress distribution in TO components, with local peak stresses induced by notches, can interact with the high surface roughness, typical of as-built AM parts, with the residual stresses, or with manufacturing defects, like pores of lack of fusion defects, which randomly forms during the AM process.[14] These interactions further complicate the analysis of the notch effect, which must be experimentally assessed, also to validate if standard methodologies

commonly employed for the fatigue design[1] can be reliably employed for AM components.

In the literature, several experimental tasks have been carried out to investigate the notch effect, the influence of the notch quality, i.e., the surface roughness in the region where peak stresses occur and the effect of post-treatments to mitigate this effect. For example, in Schnabel et al.,[15] a significant notch effect was found by testing AlSi10Mg specimens with different stress concentrations. Schnabel et al.[15] investigated the interactions between the surface roughness and the geometric notches and proved that approaches based on the effective stress computed with the critical distance theory provide reliable results, even if a large variability can be observed in the experimental data. In Nicoleto,[16] the influence of notches on the fatigue response of as-built LB-PBF AlSi10Mg specimens was verified to be strongly dependent on the building orientation and on the direction of the maximum applied stress with respect to the building orientation. Similarly, in Konecna et al.,[17] the fatigue response of AlSi10Mg specimens with semicircular notches produced with the LB-PBF process and with different building orientations was investigated. The authors found that the orientation of the semicircular notches has a significant influence, due to the different surface roughness and quality of the surface at the notch root. Moreover, the microstructure and residual stresses in the same area can influence the crack initiation and propagation stage. According to Konecna et al.,[17] the resulting fatigue response can be thus considered affected by a macro-geometrical contribution (the notch geometry) and a micro-geometrical contribution, dependent on the building direction and, accordingly, on the notch quality.

The research activity in Maleki et al.[18] focused on the effect of the T6 heat treatment and shot peening surface post-processing on the fatigue response of LB-PBF AlSi10Mg specimens with a V notch. The heat treatment and the shot peening were shown to significantly influence the fatigue response, with the latter having a prevalent effect due to its capability of inducing residual stresses and a hardened surface layer. In general, Maleki et al.[18] concluded that post-processing combined with shoot peening can effectively minimize the notch sensitivity.

In Emanuelli et al.,[19] the role of residual stresses on the fatigue response of notched LB-PBF Ti6Al4V specimens was investigated, with compressive residual stresses due to post-treatments shifting the crack initiation below the surface and with crack nucleating on the specimen surface for specimens subjected to heat treatments. The interactions between defects and notches and the role played by the highly stressed volume close to the notched region were pointed out by the authors, as confirmed also in Tridello et al.[14] through tests on a Ti6Al4V alloy up to 10^9 cycles, in the very high cycle fatigue (VHCF) life region.

In Fernandes et al.,[20] the influence of a stress relief (SR) heat treatment on the fatigue response of AlSi10Mg specimens in the high cycle fatigue (HCF) life range was investigated. Experimental results showed that the investigated SR can enhance the fatigue response and its influence varies depending on the considered life range and on the notch geometry. Similarly, in Razavi et al.,[21] LB-PBF AlSi10Mg specimens with severe notches were tested in the as-built and in the heat-treated (T6 heat treatment) condition. It was found that the applied heat treatment does not affect the notch sensitivity, with Razavi et al.[21] suggesting that surface treatments, like shot peening or ultrasonic shot peening, can be successfully employed to enhance the fatigue response.

Based on the mentioned literature, significant interactions affecting the fatigue response occur between the notch surface quality, the geometry, residual stresses, and the microstructure close to the notch tip. Furthermore, manufacturing defects or surface defects that are randomly distributed within the critical volume at the notch tip can contribute to the increment of the experimental scatter and complicate the consequent quantification of this effect. Experimental fatigue tests are therefore fundamental for investigating the notch effect, but experimental results are currently mainly limited to the low cycle fatigue (LCF) and HCF life ranges, with limited data available for the VHCF life regime.[14] However, high-performance components are required to withstand cyclic loads for a fatigue life larger than 10^7 cycles,[22–25] and therefore, the VHCF life region cannot be neglected for a safe design.

In the present paper, the influence of notch on the VHCF response of AlSi10Mg specimens produced with the LB-PBF process and with the as-built surface is investigated. Ultrasonic fatigue tests up to 10^9 cycles have been carried out on rectangular bars without notches and rectangular bars with a central through-thickness hole inducing a local stress concentration. The failure origin has been thereafter analyzed, together with micro-CT inspections investigating the defect population. The notch effect has been finally verified in a statistical framework and by

employing methodologies widely adopted for the design against fatigue failures.[1,6]

The paper aims to fill the gap of knowledge regarding the structural integrity of specimens with notch and produced with LB-PBF process, subjected to low amplitude stress for a very high number of cycles. This would enhance the comprehension of the VHCF response of LB-PBF AlSi10Mg alloy and of the influence of notch in VHCF,[26–31] whose assessment can be complex due to the interactions between the surface quality, the stress gradient and the manufacturing defects and requires appropriate experimental campaigns. All these critical factors have been considered in the analysis of the experimental data, providing general indications for the design of LB-PBF AlSi10Mg alloy even in the VHCF life region.

2 | MATERIALS AND SPECIMEN PREPARATION

In this section, the characteristics of the AlSi10Mg powder used for the specimen production and the manufacturing parameters are reported (Section 2.1). Thereafter, in Section 2.2, the specimen design procedure is described.

2.1 | Material and manufacturing process

The specimens subjected to VHCF tests are obtained starting from AlSi10Mg rectangular bars produced with an LB-PBF process by the industrial company Beam It. The powder chemical composition (average size of 45 µm) is reported in Table 1.

Bars with 40×4 mm rectangular cross-section and length equal to 150 mm are manufactured with the building orientation shown in Figure 1, i.e., with the bar longitudinal direction parallel to the building platform. Standard process parameters optimized by the Beam IT company for industrial applications have been considered. Before the removal of the specimen from the building platform, the specimens are subjected to an aging heat treatment, involving a heating temperature of 200°C for 4 h, to minimize the residual stresses without affecting the mechanical properties. Thereafter, the specimens subjected to VHCF tests, i.e., bars with rectangular cross-sections designed according to the procedure detailed in

TABLE 1 AlSi10Mg powder composition and particle size distribution (weight percentage)

Si	Mg	Cu	Ni	Fe	Mn	Ti	Al
10	0.4	<0.03	<0.05	<0.5	<0.4	<0.15	Balance
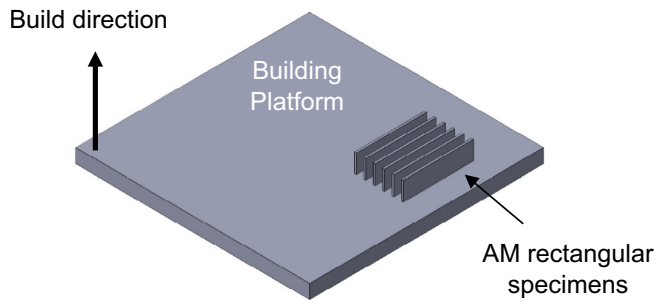
FIGURE 1 Schematic representation of the AlSi10Mg LB-PBF bars, from which the specimens subjected to ultrasonic fatigue tests have been subsequently cut, on the building platform [Colour figure can be viewed at wileyonlinelibrary.com]

TABLE 2 Quasi-static and dynamic mechanical properties of the investigated specimens

Property (unit)	Value
Dynamic Young's modulus E_{IET} (GPa)	74.5
Yield stress σ_y (MPa)	170
Ultimate tensile strength σ_{uts} (MPa)	420

Section 2.2, are cut with a Waterjet cutting machine from the AM manufactured bars.

The mechanical properties of the bars manufactured with the LB-PBF process are assessed through quasi-static tests on standard dog-bone specimens and with the impulse excitation technique (IET), according to the ASTM E1876 Standard.[32] These mechanical properties are used as input in the finite element (FE) model developed for the design of the specimens (Section 2.2) and for assessing the applied stress amplitude during the VHCF tests at 20 kHz. Table 2 reports the relevant quasi-static mechanical properties and the dynamic Young's modulus determined with the IET.

2.2 | Specimen design

In this research activity, specimens without notches (plain specimens in the following) and specimens with a hole (notch specimens in the following) are subjected to VHCF tests to investigate the notch effect on the VHCF response. The geometry of the tested specimens is defined starting from analytical formulas for rectangular bars and verified through a FE modal analysis, to ensure a resonance frequency in the range 19.5–20.5 kHz, that is the working frequency of the Ultrasonic Fatigue Testing Machine (UFTM) used for the experimental tests (Section 3.3), to verify the remoteness of proximal modes, and to assess the axial stress field within the plain and the

notch specimens. The FE modal analysis provides the ratio between the axial stress and the input displacement, which can be related to the input voltage of the experimental test for comparison with the experimental data. The FE modal analyses are performed in the LS-Dyna environment employing Belytschko-Tsay four-node shell elements with four integration points through the thickness. A mesh size equal to 0.1 mm is adopted in proximity to the notch to properly account for the stress gradient. A homogeneous elastic isotropic material law is considered according to the material properties reported in Table 2.

The geometry of the tested plain specimen is shown in Figure 2A. For the notch specimens, a through-thickness hole in the middle of the specimen, with a diameter of 2 mm, is manufactured with a milling process, as shown in Figure 2B. The stress concentration factor, K_t, due to the presence of a hole in a rectangular bar with infinite width subjected to quasi-static axial stress, is equal to 3, and it reduces to 2.52 by considering the finite width of the specimens, according to Pilkey and Pilkey.[1] On the other hand, in resonance condition at 20 kHz and with the first longitudinal mode excited in the ultrasonic fatigue test, the stress distribution can be different from the quasi-static condition, and the stress concentration due to the specimen geometry should be verified, according to Figure 2C, which shows the axial stress distribution (stress along the y direction). Accordingly, for ultrasonic fatigue tests, a dynamic stress concentration factor, $K_{t,d}$, was introduced in Tridello et al.[14] and Paolino et al.[33] For specimens with a hole, the $K_{t,d}$ factor was defined as the ratio between the peak stress and the stress far from notch at the inflection point, where the notch and the free edge counterbalance their influence and the stress amplitude becomes almost constant with respect to the x coordinate, as shown in Figure 2D. In Figure 2D, a reference system with the origin at the center of the hole and the x axis perpendicular to the longitudinal direction (y axis) is defined. According to this definition, the $K_{t,d}$ for the tested specimens is equal to 2.645. Therefore, the K_t and $K_{t,d}$ values computed for the quasi-static and the ultrasonic testing conditions are similar, with a limited difference smaller than 5%.

The possible occurrence of buckling critical stresses during the compression phase, due to the specimen geometry, is also verified with a FE analysis. An implicit buckling analysis is performed, with the displacement field of the longitudinal vibrational mode determined through the modal analysis applied to each node of the FE model. In particular, the displacement field obtained from the modal analysis is first normalized and, for the buckling analysis, multiplied by the maximum input displacement provided by the machine, i.e., the input displacement at the maximum voltage, corresponding to
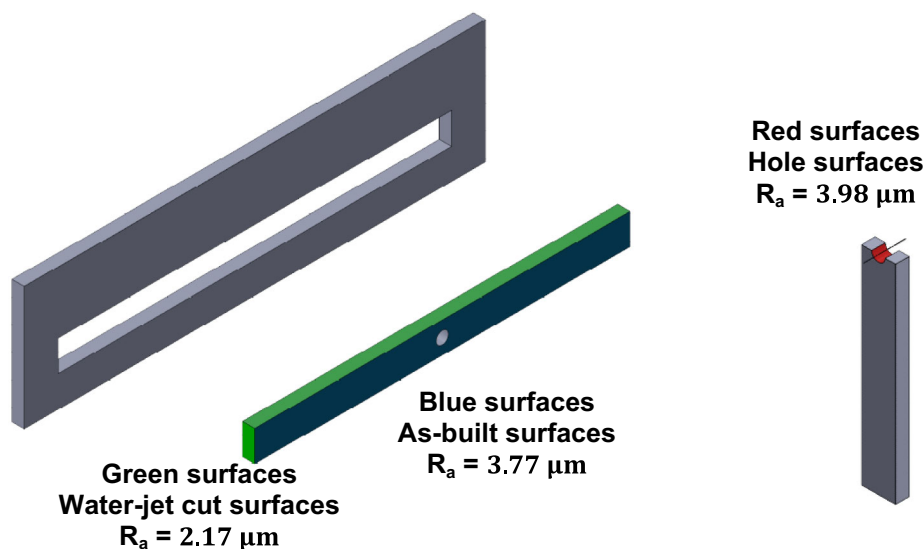
FIGURE 2 Specimens subjected to ultrasonic fatigue tests, geometry and stress distribution: (A) plain specimen geometry; (B) notch specimen geometry; (C) stress distribution in the notch specimen obtained with FE analysis (stress along the y direction); and (D) axial stress distribution along the x coordinate and definition of dynamic stress concentration factor, $K_{t,d}$ [Colour figure can be viewed at wileyonlinelibrary.com]
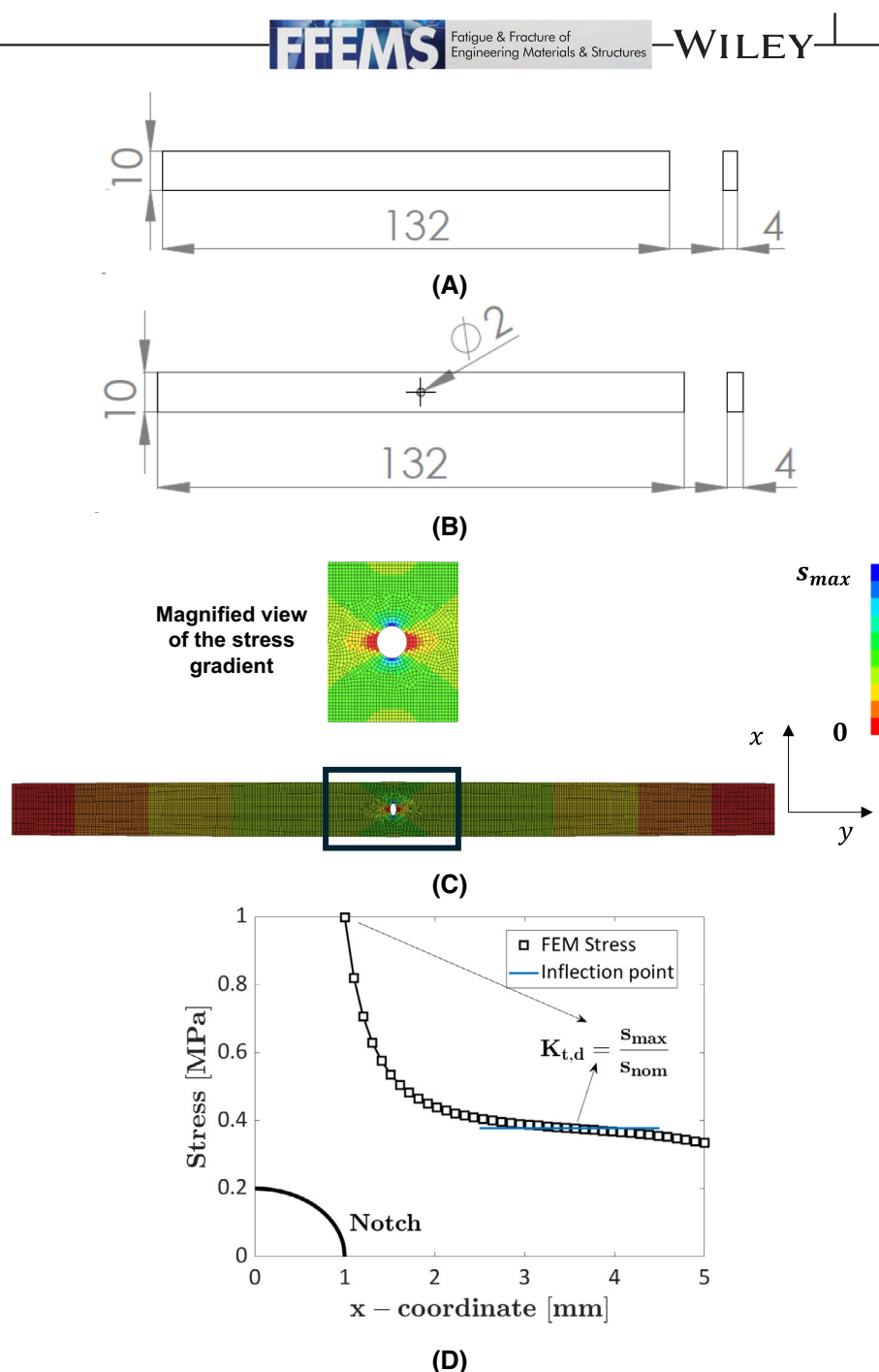
0.1 mm in the considered configuration. The results of a buckling analysis are the eigenvalues of the system, also called buckling factors, in the loaded configuration. As multiple buckling modes can occur at increasing load levels, only the first buckling factor, i.e., the first eigenvalue, has been retained. As the buckling load is the eigenvalue times the applied load, the buckling factor can be therefore seen as a safety factor against buckling. The first buckling load factor resulted equal to 1.9 for the notched specimen. Moreover, it is worth remarking that the ultrasonic tests are not performed with the maximum input displacement. Therefore, it can be concluded that buckling is not critical for the investigated configuration.

The roughness of the tested specimens on relevant surfaces is also measured with a Taylor Hobson Intra Touch 3D Profilometer. Figure 3 shows the regions where the roughness is measured. The roughness within the hole has been measured by cutting the notch specimen in correspondence of the hole, to obtain two specimen halves and allow the use of the profilometer. The Ra (arithmetic average height of the profile), the Rt (mean maximum height between the highest peak and deepest valley over five sampling lengths), Rv (mean maximum valley depth over five sampling lengths), and Rp (mean maximum peak height over five sampling lengths) parameters have been measured, as well as the

Red surfaces Hole surfaces
R_a = 3.98 μm

Blue surfaces As-built surfaces
R_a = 3.77 μm

Green surfaces Water-jet cut surfaces
R_a = 2.17 μm

FIGURE 3 Surface roughness analysis: measurement location and corresponding Ra values [Colour figure can be viewed at wileyonlinelibrary.com]

TABLE 3 Roughness parameters on the three inspected surfaces

Profile parameters				
	Ra (μm)	Rt (μm)	Rv (μm)	Rp (μm)
Water-jet cut	2.17	14.90	6.08	5.58
As built surfaces	3.77	31.30	8.85	13.00
Hole surface	3.98	21.80	8.80	9.95
Surface (2D) parameters				
	Sa (μm)	St (μm)	Sv (μm)	Sp (μm)
Water-jet cut	2.51	19.60	10.20	9.36
As built surfaces	7.57	68.80	32.40	36.40

corresponding surface (2D) roughness parameter Sa, St, Sv, and Sp. The surface (2D) roughness parameters have been measured only for the green (Water-jet cut surface) and the blu surface (as-built surface) since accurate measurements in an area cannot be obtained within the hole due to its small size and curvature. The results of the roughness analysis are reported in Table 3.

According to Figure 3 and Table 3, the Ra value of the lateral surfaces, cut with the waterjet cutting machine, is equal to 2.17 μm, whereas the Ra value inside the hole is larger and equal to 3.98 μm. The Ra value on the specimen surfaces (blue surface in Figure 3), corresponding to the as-built surface, is equal to 3.77 μm. Therefore, the hole and the as-built surfaces are characterized by similar Ra values, significantly larger than that of the water jet cut surface. On the other hand, the Rt and the Rp parameters are larger for the as-built surface. By considering the surface (2D) measurements, the difference between the water jet cut surfaces and the as-built surface is more evident. To conclude, regardless of the considered roughness parameter, the as-built and the hole surfaces are characterized by the largest roughness and, as a consequence, by the more irregular surfaces, which represent the weakest regions from which the crack is expected to originate.

3 | EXPERIMENTAL ACTIVITY

In this section, the experimental activity is described. Sections 3.1 and 3.2 focus on the defect analysis with micro-CT inspections and the microstructural characterization, respectively. In Section 3.3, the UFTM and the test configuration are described.

3.1 | Computed tomography inspection (micro-CT)

X-ray computed tomography examinations are conducted utilizing a specialized setup available within the J-Tech@PoliTO research facilities. This setup comprises a

—WILEY—

FIGURE 4 (A) Illustration of EBSD system components and sample placement and (B) the tilted sample holder with the surface prepared for analysis [Colour figure can be viewed at wileyonlinelibrary.com]
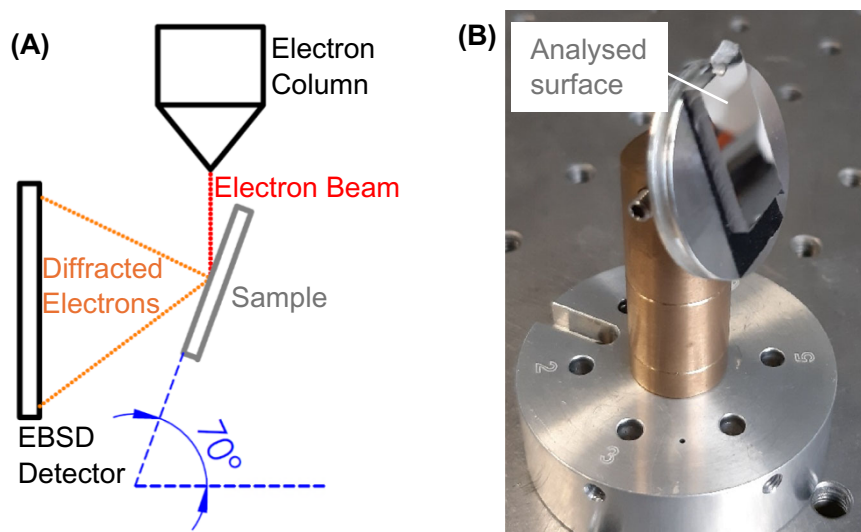
300 kV X-ray emitter and a minimum focal spot size of 5 μm, alongside a flat panel detector featuring a resolution of 2,048 × 2,048 pixels. The distance between the emitter and sample, and between the emitter and the detector, is adjusted to achieve optimal resolution.

For the specimen analysis, the scanning parameters are fine-tuned, resulting in optimal settings of 200 kV and 100 μA, generating an electron beam nominal power of 20 W. Throughout the tomography acquisition process, the distance between the X-ray source and the specimen stands at 100 mm, while the distance between the source and the detector is set at 1500 mm, resulting in a final resolution of 25 μm per voxel. To improve image quality, a physical filter consisting of 0.4 Cu is employed on the X-rays, effectively eliminating low-intensity radiation and reducing noise during the subsequent reconstruction phase.

The reconstructed three-dimensional volume of the investigated specimens is obtained employing the filtered back-projection algorithm via VG MAX 3.5 software (Volume Graphics GmbH, Heidelberg, DE), utilizing a total of 1,600 X-ray projections. In post-processing, the porosity within the analyzed specimens is identified and characterized, considering both dimensions and spatial distribution within the specimens. To ensure that only internal defects are considered, the algorithm is instructed to search for defects at a minimum distance of 30 μm, thereby excluding superficial imperfections.

Micro-CT analyses are carried out on plain and notch specimens before and after the ultrasonic fatigue tests, to investigate the fatigue crack. The inspections specifically target the central zone of each specimen, with a particular focus on a 10 mm height zone spanning the entire thickness and width of the specimens.

3.2 | Microstructural characterization

The crystallographic structure of the AlSi10Mg specimens is investigated through the EBSD analysis, using the Oxford Instruments AZtec EBSD system incorporated into a Field Emission Scanning Microscope (FESEM) Tescan MIRA3.

For the EBSD analysis, the notch specimens are mechanically polished in the plane perpendicular to the notch axis (blue surface in Figure 3) with a Presi Mecatech 250 SPI polishing machine, using sandpapers from #180 to #1200 grit, polishing cloths imbued with diamond suspensions with crystal sizes from 9 μm down to 1 μm, and finished with a cloth imbued in colloidal silica suspension with particle size of 0.3 μm. The surface is then cleaned in an ultrasonic bath of isopropanol at ambient temperature to remove the remaining silica particles.

For the EBSD analysis, the sample is placed inside the FESEM with the analyzed surface at a 70° angle with respect to the horizontal plane and facing the EBSD detector, as shown in Figure 4A. The electrons diffracted by the sample surface are then received by the detector, allowing a crystallographic map to be generated. Maps are acquired from the prepared surfaces, as shown in Figure 4B, both in the vicinity of the notch, as well as in areas away from the hole.

The general parameters used for map acquisition are shown in Table 4. The only non-fixed parameter between the different scans is the magnification, which in turn affects the admissible step size; i.e., the higher the magnification, the smaller the minimum step size. In particular, the "resolution" parameter used by the AZtec software represents the number of pixels of the side of the observed square area, which comprises an EBSD map,

TABLE 4 Parameters adopted in the acquisitions of the EBSD maps

Parameter	Value
High voltage	20 kV
Beam intensity	16
Working distance	~15 mm
Magnification	Between 250× and 500×
Dwell time	35 μs
Resolution	2,048 pixels
Step size	Between 0.2 and 0.4 μm

representing a different quantity than the "resolution" parameter employed by the software VG MAX in the CT scan analyses, which is defined in Section 3.1.

Additionally, with the Oxford Instruments AZtec EDS (Energy Dispersive X-ray Spectroscopy) system, the chemical compositions of all the areas analyzed through EBSD are also acquired, to assess the weight percentages of the chemical elements present on the analyzed surface.

3.3 | Ultrasonic fatigue tests and stress validation

The ultrasonic fatigue tests have been carried out up to 10^9 cycles (runout number of cycles) to investigate the influence of notch on the VHCF response of the tested AlSi10Mg alloy. The UFTM developed at the Politecnico di Torino is used, with ultrasonic fully reversed tension-compression tests carried out. The experimental tests are carried out in displacement-controlled mode, with the displacement amplitude at the specimen-free end measured with a laser displacement sensor (LK-G5001P laser from Keyence Corporation) and used as the feedback control signal. Similarly, the temperature close to the specimen center is measured with an infrared sensor and kept below 25°C with two vortex tubes.[34]

The stress in the notched specimens has been measured close to the hole (Gage 1) and close to the lateral border (Gage 2) from the strains provided by micro-strain gages (HBM 1-LY11-0.3/120) with a grid length of 0.3 mm, as shown in Figure 5A. In particular, Gage 1 is bonded as close as possible to the hole, whereas Gage 2 is bonded as close as possible to the specimen external border. Figure 5B shows the applied stress amplitude with respect to the voltage in output from the piezoelectric transducer. Figure 5C plots the experimental stress amplitude, s_a, with respect to the FE stress amplitude, for Gages 1 and 2.

According to Figure 5B, the experimental stress amplitude follows a linear trend with respect to the input voltage, as expected. The stress amplitudes acquired by Gage 1 are above the stress amplitudes acquired by Gage 2, with a different slope. The ratio between the stress amplitude measured by Gages 1 and 2 does not correspond to the $K_{t,d}$ value obtained in Section 2.2, since the stress amplitudes acquired by Gage 1 are below the peak stress. The experimental and the FE stress amplitudes at the strain gage locations were compared. According to Figure 5C, the experimental stress amplitudes are close to the FE stress amplitudes for the same applied voltage, with the data concentrated close to the bisector. Therefore, the FE model is validated, and the $K_{t,d}$ value computed with the FE is confirmed.

4 | EXPERIMENTAL RESULTS

In this section, the experimental results are analyzed. In Section 4.1, the results of the ultrasonic fatigue tests are reported. Section 4.2 focuses on the microstructural characterization with the EBSD detector and on the results of the defect analysis with micro-CT inspections and by analyzing the fracture surfaces. Finally, in Section 4.3, the experimental results are analyzed in a probabilistic framework, pointing out the differences between the notch effect in standard fatigue tests and in ultrasonic fatigue tests.[35,36]

## 4.1 | Ultrasonic fatigue test results

In this section, the experimental results are reported. Figure 6 plots the experimental data (nominal stress amplitude) in an S-N plot. The round markers are the failures, whereas the triangle markers are the runout at 10^9 cycles. The S-N curves are also estimated, by assuming the logarithm of the fatigue life as normal, with the mean linearly dependent on the logarithm of the applied stress amplitude and constant standard deviation.[37] The parameter estimation is carried out by applying the Maximum Likelihood Principle and by considering both failure and runout data. The median, the 0.1-th, and the 0.9-th quantile P-S-N curves are plotted in Figure 6 for the notch and plain specimens.

According to Figure 6, the notch effect is evident, with the data obtained by testing plain specimens failing at stress amplitudes significantly larger, for the same applied number of cycles to failure. The runout data also confirm this trend, with no failures below 50 MPa for the notch specimens and no failures below 75 MPa for the plain specimens. Moreover, the 80% P-S-N curve
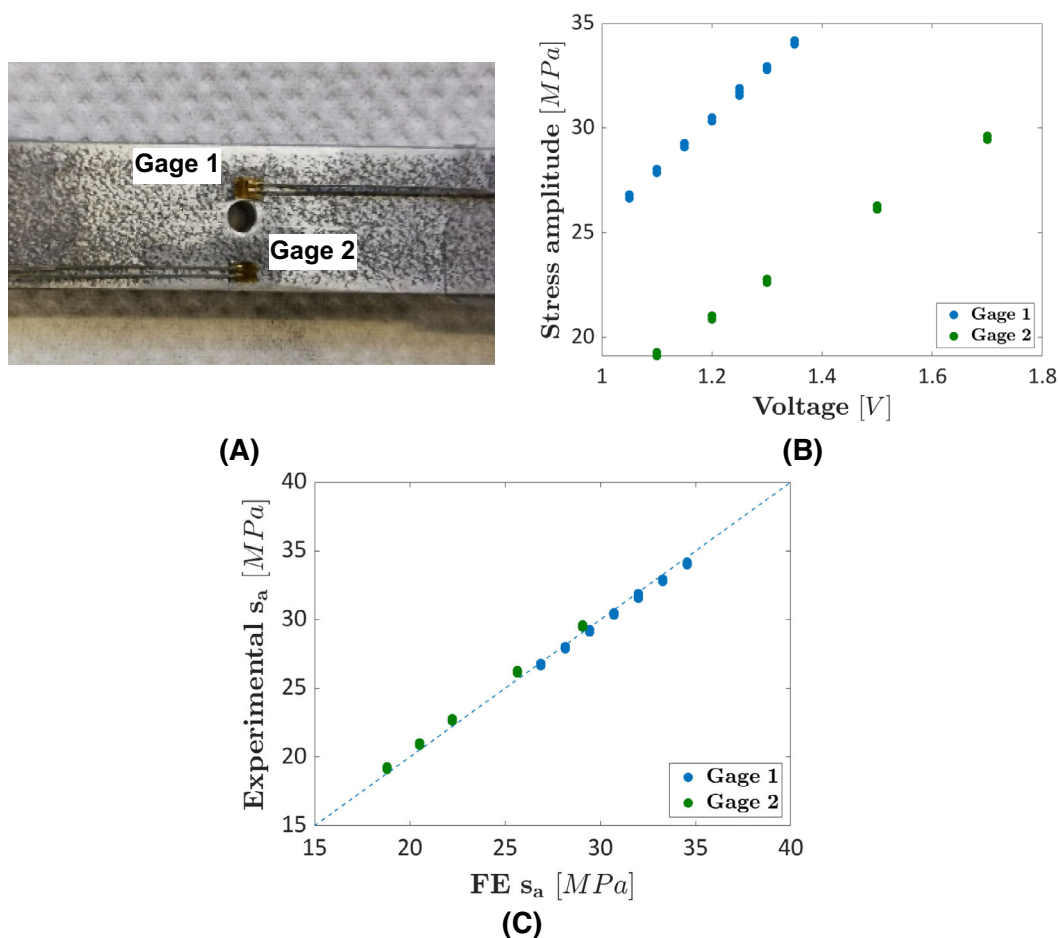
FIGURE 5 Validation of the applied stress amplitude with strain gages: (A) strain gages bonded to the specimens; (B) applied stress amplitude with respect to the input voltage exerted by the piezoelectric transducer; and (C) experimental stress amplitude with respect to the stress amplitude computed with FE [Colour figure can be viewed at wileyonlinelibrary.com]

FIGURE 6 S-N plot of the experimental results and estimated median, 0.1-th and 0.9-th quantile P-S-N curves [Colour figure can be viewed at wileyonlinelibrary.com]
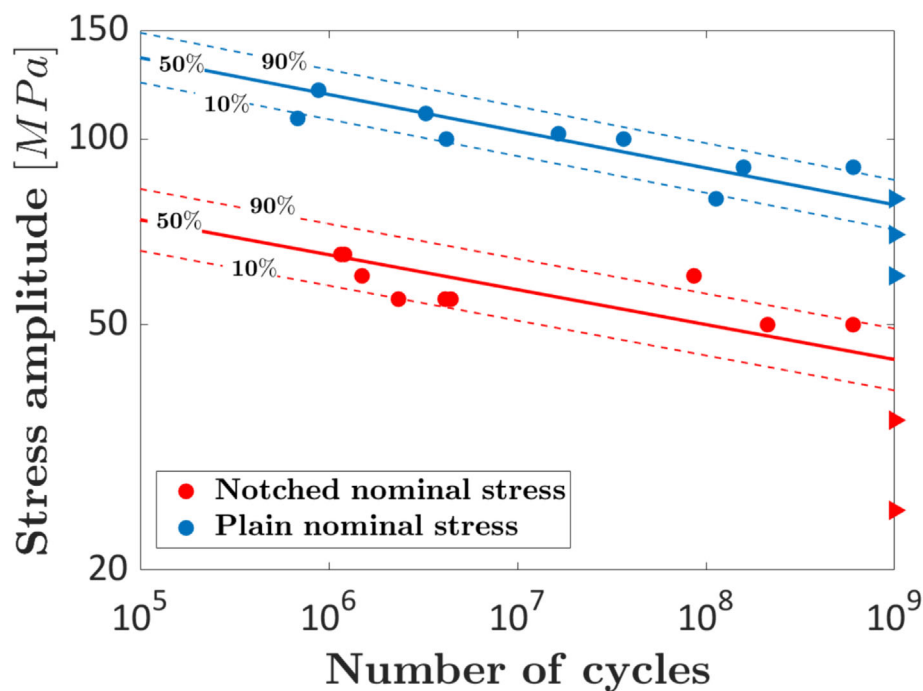
intervals do not overlap, further proving the significant difference. It can be noted that the slope of the two S-N curves is almost the same, with limited differences. Indeed, as discussed in the following sections, the failure origin is the same, with surface defects due to the high surface roughness controlling the fatigue response for both investigated conditions. Accordingly, the slope is not expected to significantly vary. It must be also noted that the slope is strongly dependent on the distribution of the experimental data within the investigated life range and the dataset numerosity. Accordingly, if a larger (or a smaller) amount of data were available, the slopes would be different, but this difference would not be expected to be very high due to the same failure origin.

The scatter is large for both specimens: for example, for an applied stress amplitude of 60 MPa, failures range from 1.5×10^6 cycles to 8.6×10^7 cycles for notch specimens. Similarly, for an applied stress amplitude of 100 MPa, failures range from 4.2×10^6 cycles to 3.67×10^7 cycles for plain specimens. The reason for the experimental scatter, which is typical for AM specimens and is generally larger than that of traditionally built specimens due to the interaction between defects, stress gradient, and surface roughness, is investigated in the following sections.

4.2 | Microstructural characterization and defect analysis

In this section, the results of the microstructural characterization and the defect analysis are analyzed. In detail, Section 4.2.1 focuses on the EBSD analysis, whereas Section 4.2.2 is about the defect characterization, with micro-CT inspections and micrographs of the fracture surfaces with the FESEM.

4.2.1 | Microstructural analyses

Figure 7 shows the results of the EBDS analysis. In particular, Figure 7A shows the measurement locations; Figure 7B,C shows the crystallographic map close to the notch (location *a*) and at the same axial position but in a location where the notch has no effect (location *b*), respectively. In general, according to Figure 7B,C, it can be concluded that the microstructure and the grain distribution and size are not affected by the measurement location. Indeed, the grains in the vicinity of the notch have approximately the same characteristics in terms of size range, average size, and general shape, as those assessed in the areas far away from the notch.

Figure 7b,c shows irregularly shaped grains with large size variability, in agreement with literature data for AlSi10Mg, as reported in Konecna et al.[17] and Yang et al.[38] To highlight this variability, the grain size range, average, and standard deviation are reported in Table 5, for the analyses carried out in the vicinity of the notch and far from it, with a total of four maps acquired for each type of area. The results in Table 5 exclude the grains located on the borders of the maps, as their areas are not entirely captured in the respective analyses. Furthermore, the results of the analysis of the chemical composition are reported in Table 5, showing that the percentages of silicon and magnesium are within the expected values for AlSi10Mg.
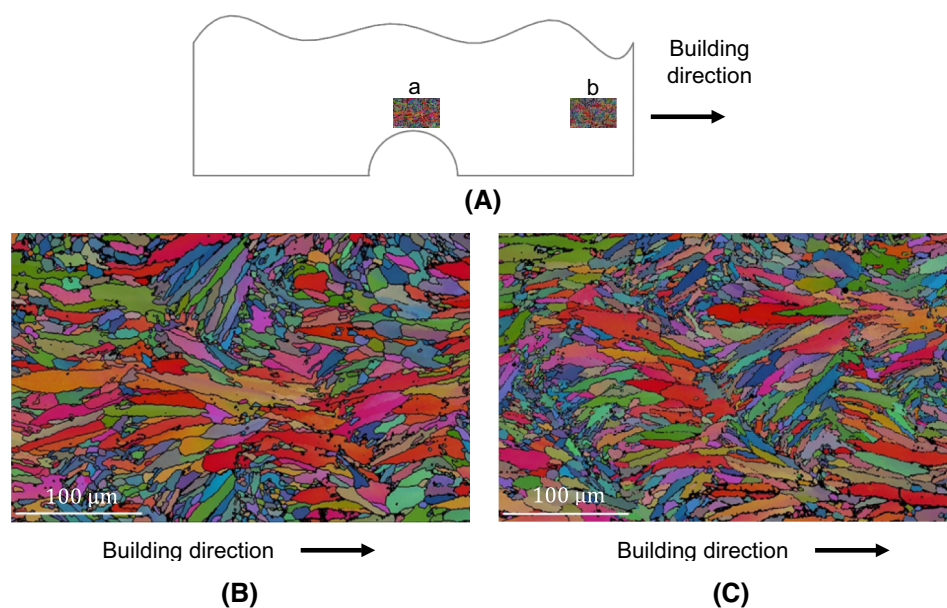
FIGURE 7 EBSD analysis: (A) measurement location; (B) EBSD map at location a; and (C) EBSD map at location b [Colour figure can be viewed at wileyonlinelibrary.com]

Although the standard deviations for the measured grain sizes are different in locations a and b, no correlation between the standard deviation and the measuring location can be established. Indeed, for the four maps acquired around the notch area, the standard deviations ranged from 56.3 to 132.7 μm^2, while the four maps on areas without notch effect had standard deviations between 58.8 and 122.9 μm^2. Since the grain size range for all areas is quite large, being comprised in the range of [2, 1,200] μm^2 in all observations, the difference in variability among the maps is considered intrinsic to the production process and cannot be considered significant.

Table 5 confirms that the specimen microstructure does not vary with the measurement location, in line with the data reported by Konecna et al.,[17] which pointed out that the fatigue life in notched AlSi10Mg specimens is mainly influenced by the quality of the notch surface and the specimen build orientation since the presence of the notch does not cause local microstructural alterations. In general, however, it is expected that grain size, shape, and orientation influence notch sensitivity in fatigue tests, as shown in Lorenzino and Navarro,[39] which analyzed grain size effect on notch sensitivity of Aluminum 1050. According to this study, notch sensitivity tends to be reduced when grain size is increased. Since Lorenzino and Navarro[39] used laminated aluminum sheets to produce the specimens, as well as controlled thermomechanical treatments to alter grain size, the observed grains tend to have more uniform shapes and size distributions than the grains observed in Figure 7. However, it is reasonable to assume that, in the tested LB-PBF AlSi10Mg specimens, smaller grains, of areas down to around 3 μm^2, affect the fatigue response close to the notch. On the other hand, due to the random distribution of grain size, and the random and rare occurrence of small grains, the influence of these small grains can be considered limited, with the fatigue response mainly controlled by surface defects and irregularities.

4.2.2 | Defect analysis

In this section, the defect population is investigated by analyzing the results of the micro-CT inspections and the defects at the origin of the fatigue failures on the fracture surface. Figure 8 plots the internal defect sphericity with respect to the square root of the area of the defects projected in a plane perpendicular to the direction of the maximum applied stress ($\sqrt{Area}$), according to Murakami.[40]

According to Figure 8, the sphericity tends to decrease with the defect size, in agreement with Colombo et al.,[41] Larrosa et al.,[42] and Wu et al.[43] Indeed, larger defects tend to have a more irregular shape. The size of internal defects is close to that found in the literature for AlSi10Mg specimens subjected to fatigue tests.[42–44] The maximum defect is characterized by a $\sqrt{Area}$ smaller than 130 μm, below that found in Tridello et al.,[44] where defects with an $\sqrt{Area}$ above 200 μm were detected. However, the defect population is strongly dependent on the specimen geometry and on the process parameters selected for manufacturing the specimens,[45] thus explaining this difference in the size of the defects.

A second analysis is carried out with micro-CT. Indeed, in ultrasonic fatigue tests, the test ends when the specimen

TABLE 5 EBSD and EDS analysis results for areas at location *a* and location *b*

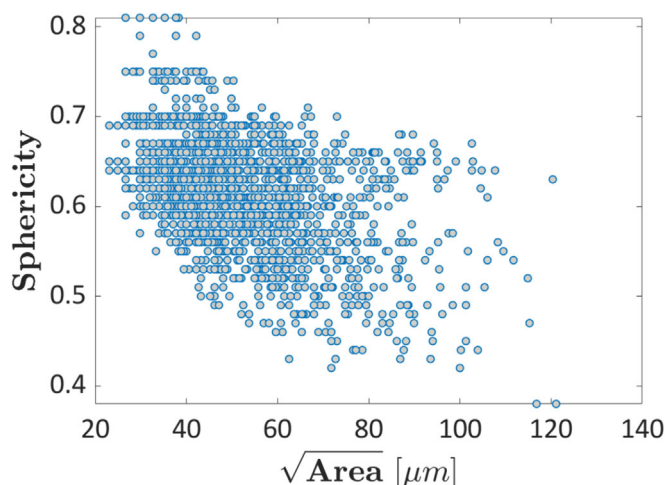| EBSD statistic data		
Analysis location	**Location a**	**Location b**
Minimum grain area (μm^2)	3.1	2.6
Maximum grain area (μm^2)	936.4	866.2
Average grain area (μm^2)	35.9	42.0
The standard deviation of grain area (μm^2)	74.9	95.7
EDS chemical composition—weight percentages		
Aluminum (%)	89.59	89.49
Silicium (%)	9.38	9.41
Magnesium (%)	0.87	0.93
Iron (%)	0.17	0.17

FIGURE 8 Defect sphericity with respect to the square root of the defect area projected in a plane perpendicular to the direction of the maximum applied stress, $\sqrt{Area}$ [Colour figure can be viewed at wileyonlinelibrary.com]
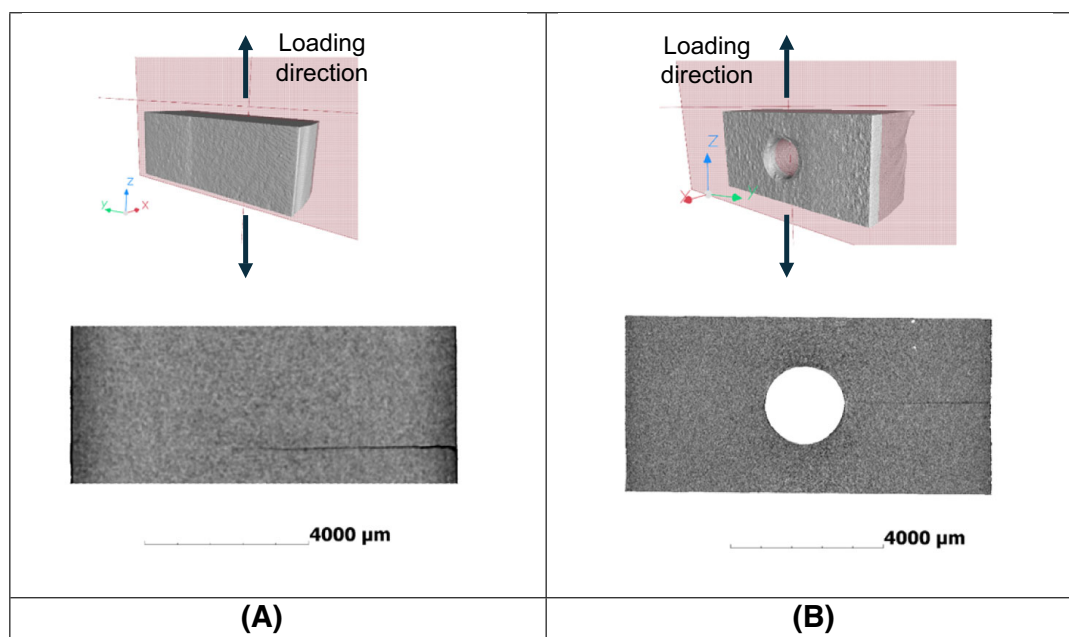
FIGURE 9 Crack visualization from CT inspection of the plain specimen (A) and the specimen with the notch (B) [Colour figure can be viewed at wileyonlinelibrary.com]

resonance frequency, due to the propagation of a fatigue crack, suddenly drops and falls outside the UFTM frequency working range [19.5:20.5] Hz. Accordingly, the test ends without a separation of the specimens into two halves. To verify the crack origin and propagation, a micro-CT inspection is carried out on a plain and a notch specimen after failure. Indeed, the crack is generally not visible on the specimen surface. Failed specimens are thereafter subjected to a quasi-static tensile test to separate them into two halves and observe the fracture surfaces with the FESEM.

For the plain specimens, a cross-section generated by a plane parallel to the loading direction (z axis) is shown in Figure 9A. The distance between the crack and the specimen center is equal to 7.95 mm. Therefore, for this specimen, the fatigue crack originated in a region close to the specimen center, i.e., where a critical surface defect due to the high roughness is present. In order to properly investigate the crack origin, the fracture surfaces are observed, as discussed in the following.

It must be noted that, in the performed analyses, the nominal applied stress amplitude, i.e., the stress amplitude at the specimen center, has been considered. Indeed, even if the failure origin is not always located at the specimen center, the local stress amplitude inducing the experimental failures is close to the maximum applied stress. For example, for the fatigue failure originating at about 8 mm from the specimen center, the difference between the local and the nominal stress is smaller than 3%. For this reason, in all analyses, the nominal stress

amplitude has been considered in place of the local stress amplitude.

In Figure 9B, the same cross-section for the notch specimen is shown. In this case, the crack is near the specimen center. In particular, it is interesting to note that the crack has initiated where the stress reaches its maximum value close to the hole, as expected, but only on one side of the hole. This can be caused by a worse hole surface quality in this region and confirms that random surface defects interacting with the stress gradient control the crack nucleation process and, accordingly, the resulting fatigue life of notched specimens.

The crack origin is finally analyzed with the FESEM. Figures 10A,B show the fracture surface of a notch specimen and of a plain specimen, respectively. According to the fatigue marks identified on the fracture surfaces, the crack originates on the specimen surface for plain specimens. Internal defects analyzed with micro-CT inspections (Figure 8) are not critical for the investigated specimens, since surface defects due to the high surface roughness have a more detrimental effect. For the notch specimens, the fatigue crack originates at the border of the notch for all tested specimens, in the local region with the maximum stress, as shown in Figure 10A. Failures are, moreover, randomly distributed along the hole thickness. Even for notch specimens, the low surface quality, interacting with the local peak stress, is responsible for the crack initiation,[46] with the internal defects being not critical. This is in agreement with literature results,[18,21] where the authors pointed out the
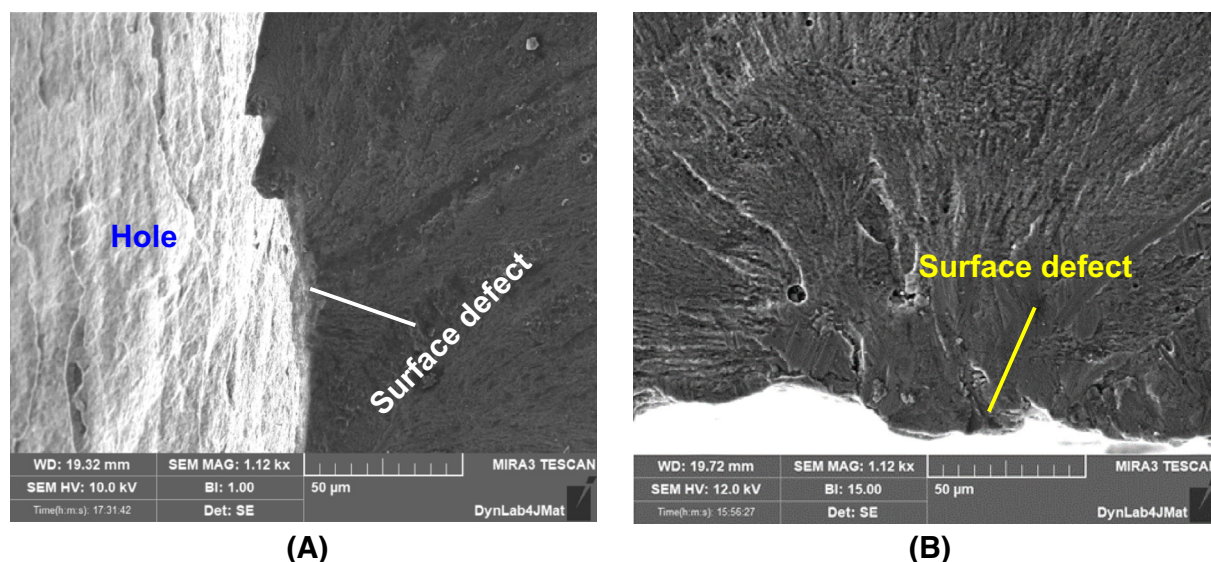
—WILEY—

FIGURE 10   Representative images of the fracture surfaces: (A) notch specimens and (B) plain specimens [Colour figure can be viewed at wileyonlinelibrary.com]

importance of improving the surface quality with appropriate post-treatments to enhance the fatigue response, especially if notches are present.

5 | DISCUSSION

According to the S-N plot reported in Figure 6, the experimental data show a quite large scatter, which can make it difficult to quantify the notch effect. Moreover, the experimental data are obtained in a large life range, between 10^6 cycles and 10^9 cycles, whereas the objective of this research activity is to focus on the notch effect in the VHCF life region. Accordingly, all the experimental failures are shifted to the reference number of cycles, N_{ref}, corresponding to 10^9 cycles, according to a common literature procedure.[47] Very briefly, starting from the statistical distribution of the fatigue life described in Section 4.1, it can be assumed that each experimental failure is crossed by a specific α-th quantile curve. Once the α-th quantile curve for the considered failure is individuated, the corresponding fatigue strength for the same quantile and N_{ref}, corresponding to 10^9 cycles, can be computed.

Figure 11 compares the fatigue strength of the shifted failures. The shifted experimental data, together with the 95% confidence interval plot for the mean, are reported.

Figure 11 confirms the significant notch effect found by analyzing the experimental data in the S-N plot. The effective fatigue notch factor,[1] computed as the ratio between the mean fatigue strength of the plain specimens and the mean fatigue strength of the notched specimens, is equal to 1.76. On the other hand, the fatigue notch
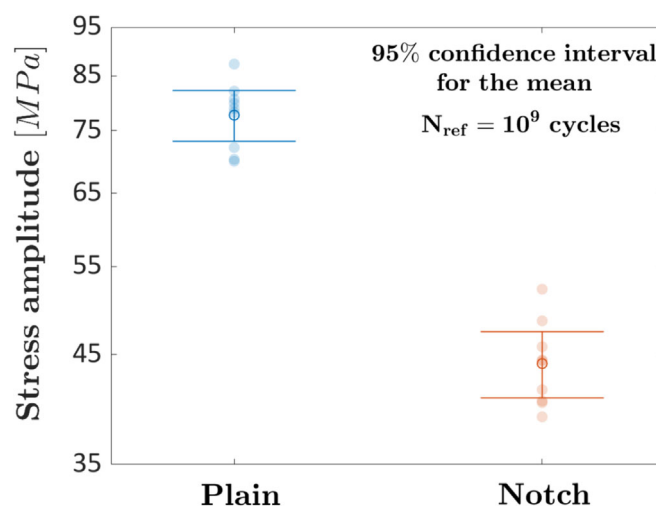
FIGURE 11   Shifted fatigue strength at the reference number of cycles to failure of 10^9 cycles, together with the 95% interval plot for the mean [Colour figure can be viewed at wileyonlinelibrary.com]

factor computed with the standard procedure reported in Pilkey and Pilkey[1] and Collins[48] and by assessing the notch sensitivity factor according to the Neuber relation (i.e., with the notch sensitivity depending on the notch radius and a material constant provided as a function of the tensile strength) has been found larger and equal to 1.87. Similarly, following the procedure reported in the FKM guidelines, where the relative stress gradient factor $\overline{G}$ can be computed from the geometry of the notch and material constants for aluminum alloys are retained, the fatigue notch factor results equal to 1.86. In the analyses based on the Neuber formula and on the FKM guidelines, the theoretical stress concentration factor for standard

tests, i.e., the one provided by the chart for a hole in a finite plate subjected to tensile stress and equal to 2.52 (Section 2), is considered. The difference between the effective notch factor and those computed with the literature relationships is close to 5% and is quite limited. It must be noted that this limited discrepancy can be attributed to the material parameters adopted for the computation of the notch factor with the theoretical methods. For example, the FKM guidelines provide parameters only for wrought aluminum alloys, whereas the microstructure of the investigated AlSi10Mg alloy is significantly different from that of wrought AlSi10Mg alloys.

Moreover, the interaction between the surface roughness and possible size effects must be discussed. The fracture surface analysis of Section 4.2.2 has shown that, for the notch specimens, the fatigue crack originates at the border of the notch, where a random defect due to high roughness along the transversal direction is present together with the local stress concentration. In plain specimens, the crack originates from the as-built surface in the central region of the specimen, where the stress amplitude reaches its maximum value and in correspondence of the largest and most critical surface irregularity. Moreover, a large volume of material is subjected to a stress amplitude close to the maximum applied stress amplitude in plain specimens (risk volume, defined as the volume of material subjected to a stress amplitude above the 90% of the maximum applied stress according to Murakami,[40] above 1,000 mm^3). Accordingly, even surface irregularities away from the specimen center can become critical. On the other hand, in notch specimens, the volume of material subjected to the peak stress is very small (risk volume, according to Murakami[40] below 1 mm^3), with size effect also playing a role.[14] Therefore, even if a significant notch effect is found, the effective K_f factor can be larger, since lowered by the surface roughness and related size effect.

To account for the experimental variability, a range for the effective fatigue notch factors is also computed. The lower limit is computed as the ratio between the 2.5% quantile and the 97.5% quantile of the mean fatigue strength of the plain and notched specimens, respectively. Similarly, the upper limit for the notch fatigue factor has been computed as the ratio between the 97.5% quantile and the 2.5% quantile of the fatigue strength of the plain and notched specimens, respectively. The resulting interval is [1.54:2.04], including the notch fatigue factor computed with standard literature methodologies employed for the design of traditionally built specimens. The widely adopted methodologies for the quantification of the notch effect have therefore proven to be effective, on average, even for the VHCF life range obtained at ultrasonic frequency and for AM parts with as-built surfaces. However, the range for the effective

fatigue notch factor is quite large and experimental validation of the fatigue notch factor is recommended.

It must be noted that residual stresses may have formed close to the notch after the drilling process. The surface roughness and the local peak stress due to the notch play the most relevant role and mainly affect the VHCF response of the investigated specimens, with the residual stresses contributing to the experimental scatter observed in the S-N plot. The influence of the residual stress is expected to fall within the estimated quantile P-S-N curve ranges or the 95% confidence intervals for the fatigue strength at 10^9 cycles, pointing out the importance of properly modeling the experimental variability and not relying on mean or median values, with the estimated scatter intervals including factors which are not under control.

6 | CONCLUSION

In the research activity carried out in this paper, the influence of notch on the fatigue response of AlSi10Mg specimens produced with the LB-PBF process is investigated. Ultrasonic fatigue tests up to 10^9 cycles have been carried out on bars with rectangular cross-sections with a through-thickness hole (2 mm diameter hole in a width of 10 mm, notch specimens in the following) at the center of the specimen, and without the hole (plain specimens). The following conclusions can be drawn:

- The dynamic stress concentration factor, introduced for ultrasonic fatigue tests, and defined for the tested specimens as the ratio between the maximum stress close to the notch and the stress at the inflection point of the stress trend, where the notch and the free edge counterbalance their influence, is equal to 2.64, with a discrepancy from the value found for a hole in a finite plate and subjected to conventional axial fatigue tests smaller than 5%.
- The local stress concentration induced by the notch has a significant effect on the VHCF response. The 80% interval curves of plain specimens are above the 80% interval curves for the notched specimen with no overlap, thus indicating a significant notch effect.
- Failures originate from the specimen surface in plain specimens, where the surface roughness due to the as-built condition is the highest. In the notched specimen, the fatigue failures originate at the border of the notch, where the stress concentration is present, and from a random surface irregularity. Internal defects, on the other hand, are not critical.
- The experimental notch fatigue factor at 10^9 cycles, $K_{f,exp}$, is equal to 1.76 and is close to the theoretical notch fatigue factor ($K_{f,th} = 1.86$), computed with

widely employed literature models, with a limited difference smaller than 5%. Moreover, the range of variation of $K_{f,exp}$, computed by taking into account the experimental variability, is quite large and equal to [1.54: 2.04], which includes the $K_{f,th}$ computed with literature models. Therefore, literature models can be employed to quantify the notch effect of as-built AM parts subjected to VHCF loads, but experimental tests are recommended due to the large range of the $K_{f,exp}$ values.

- Notch effect and surface quality interact and affect the crack initiation process. The experimental activity has proven that even very low-stress amplitudes, which can be considered safe during the design stage, can be critical and originate a fatigue failure if applied for a very high number of cycles.

NOMENCLATURE

E_{IET}	dynamic Young's modulus
$\overline{G}$	relative stress gradient factor
$K_{f,exp}$	effective fatigue notch factor
K_t	theoretical stress concentration factor
$\sqrt{area}$	square root of the area of the defect projected in a plane perpendicular to the maximum applied stress amplitude
σ_{uts}	ultimate tensile strength
σ_y	yield stress
$K_{t,d}$	dynamic stress concentration factor
R_a	surface roughness (arithmetic mean roughness)
s_a	stress amplitude

AUTHOR CONTRIBUTIONS

Andrea Tridello: Methodology; investigation; data curation; project administration; supervision; formal analysis; writing—original draft preparation. **Carlo Boursier Niutta:** Methodology; investigation; data curation; formal analysis; writing—original draft preparation. **Alessandro Benelli:** Methodology; investigation; data curation; writing—original draft preparation. **Ana Paula Pagnoncelli:** Methodology; investigation; data curation; writing—original draft preparation. **Massimo Rossetto:** Resources; writing—review and editing; supervision. **Filippo Berto:** Resources; writing—review and editing; supervision. **Davide Salvatore Paolino:** Resources; writing—review and editing; supervision.

ACKNOWLEDGEMENTS

DATA AVAILABILITY STATEMENT

The data that support the findings of this study are available from the corresponding author upon reasonable request.

ORCID

Andrea Tridello https://orcid.org/0000-0003-3007-3377
Carlo Boursier Niutta https://orcid.org/0000-0002-7894-4752
Alessandro Benelli https://orcid.org/0000-0002-4202-8023
Ana Paula Pagnoncelli https://orcid.org/0000-0001-7171-5255
Filippo Berto https://orcid.org/0000-0001-9676-9970
Davide Salvatore Paolino https://orcid.org/0000-0002-4231-4580

REFERENCES

1. Pilkey WD, Pilkey DF. *Shoulder Fillets*. Wiley; 2007.
2. Liao D, Zhu SP, Correia JAFO, de Jesus AMP, Berto F. Recent advances on notch effects in metal fatigue: a review. *Fatigue Fract Eng Mater Struct*. 2020;43(4):637-659.
3. Zanichelli A, Ronchei C, Scorza D, Vantadori S. Fatigue lifetime of both plain and notched specimens made of additively manufactured AISI 316L. *J Mater Res Technol*. 2022;21:2532-2546.
4. Ronchei C, Vantadori S. Notch fatigue life estimation of Ti-6Al-4V. *Eng Fail Anal*. 2021;120:105098.
5. Zhu SP, Xu S, Hao MF, Liao D, Wang Q. Stress-strain calculation and fatigue life assessment of V-shaped notches of turbine disk alloys. *Eng Fail Anal*. 2019;106:104187.
6. Haibach E. FKM-guideline: analytical strength assessment of components in mechanical engineering (5th Reved.), English version. Germany, Frankfurt/Main: Forschungskuratorium Maschinenbau. 2003.
7. Siebel E, Stieler M. Significance of dissimilar stress distributions for cycling. *VDI-Zeitschrift*. 1955;97:121-126.
8. Zhu SP, Ye WL, Correia JAFO, Jesus AMP, Wang Q. Stress gradient effect in metal fatigue: review and solutions. *Theor Appl Fract Mech*. 2022;121:103513.
9. Rosen DW, Gibson I, Stucker B. Additive manufacturing technologies.2015.
10. Berrocal L, Fernández R, González S, et al. Topology optimization and additive manufacturing for aerospace components. *Prog Addit Manuf*. 2019;4(2):83-95.
11. Liu J, Gaynor AT, Chen S, et al. Current and future trends in topology optimization for additive manufacturing. *Struct Multidiscip Optim*. 2018;57(6):2457-2483.
12. Zhu J, Zhou H, Wang C, Zhou L, Yuan S. A review of topology optimization for additive manufacturing: status and challenges. *Chinese J Aeronaut*. 2021;34(1):91-110.
13. Roschli A, Gaul KT, Boulger AM, et al. Designing for big area additive manufacturing. *Addit Manuf*. 2019;25:275-285.
14. Tridello A, Boursier Niutta C, Berto F, Paolino DS. Blunt notch effect on the fatigue response up to 109 cycles of selective laser melting Ti6Al4V specimens. *Fatigue Fract Eng Mater Struct*. 2023;46(9):3417-3428.
15. Schnabel K, Baumgartner J, Möller B, Scurria M. Fatigue assessment of additively manufactured AlSi10Mg structures using effective stress concepts based on the critical distance approach. *Weld World*. 2021;65(11):2119-2133.
16. Nicoletto G. Influence of rough as-built surfaces on smooth and notched fatigue behavior of L-PBF AlSi10Mg. *Addit Manuf*. 2020;34:101251.

17. Konecna R, Nicoletto G, Kunz L, Jambor M. Notch orientation and fatigue strength of as-built L-PBF AlSi10Mg. *Procedia Struct Integr.* 2022;42:857-862.

18. Maleki E, Bagherifard S, Razavi N, et al. Fatigue behaviour of notched laser powder bed fusion AlSi10Mg after thermal and mechanical surface post-processing. *Mater Sci Eng A.* 2022;829:142145.

19. Emanuelli L, Molinari A, Facchini L, et al. Effect of heat treatment temperature and turning residual stresses on the plain and notch fatigue strength of Ti-6Al-4V additively manufactured via laser powder bed fusion. *Int J Fatigue.* 2022;162:107009.

20. Fernandes RF, Jesus JS, Borrego LP, Ferreira JAM, Costa JD. Notch effect on the fatigue behaviour of AlSi10Mg aluminium alloy obtained by additive manufacturing. *Proc Struct Integr.* 2024;54:300-306.

21. Razavi N, Bagherifard S, Hafnor S, Spiller S, Guagliano M, Berto F. Fatigue analysis of as-built and heat-treated severely notched AlSi10Mg alloy specimens made by laser powder bed fusion technology. *Int J Fatigue.* 2024;179:108041.

22. Bathias C, Paris PC. Gigacycle fatigue of metallic aircraft components. *Int J Fatigue.* 2010;32(6):894-897.

23. Bathias C, Paris PC. *Gigacycle Fatigue in Mechanical Practice.* CRC Press; 2004.

24. Bayraktar E, Garcias IM, Bathias C. Failure mechanisms of automotive metallic alloys in very high cycle fatigue range. *Int J Fatigue.* 2006;28(11):1590-1602.

25. Shanyavskiy AA. Very-high-cycle-fatigue of in-service air-engine blades, compressor and turbine. *Sci China Phys Mech Astron.* 2014;57(1):19-29.

26. Akiniwa Y, Miyamoto N, Tsuru H, Tanaka K. Notch effect on fatigue strength reduction of bearing steel in the very high cycle regime. *Int J Fatigue.* 2006;28(11):1555-1565.

27. Qian G, Hong Y, Zhou C. Investigation of high cycle and very-high-cycle fatigue behaviors for a structural steel with smooth and notched specimens. *Eng Fail Anal.* 2010;17(7-8):1517-1525.

28. Himmelbauer F, Winter G, Grün F, Kiesling C. VHCF properties and assessment of specimens and thin-walled component-like structures made of high-strength steel X5CrNiCuNb16-4. *Int J Fatigue.* 2022;156:106645.

29. Shen J, Fan H, Zhang G, Pan R, Wang J, Huang Z. Influence of the stress gradient at the notch on the critical distance and life prediction in HCF and VHCF. *Int J Fatigue.* 2022;162:107003.

30. Gao Z, Chen X, Zhu S, He Y, Xu W. Notch fatigue behavior of a titanium alloy in the VHCF regime based on a vibration fatigue test. *Int J Fat.* 2023;172:107608.

31. Dantas R, Gouveia M, Silva FGA, et al. Notch effect in very high-cycle fatigue behaviour of a structural steel. *Int J Fatigue.* 2023;177:107925.

32. E1876–22 A. Standard test method for dynamic Young's modulus, shear modulus, and Poisson's ratio by impulse excitation of vibration 1. 2022.

33. Paolino DS, Tridello A, Chiandussi G, Rossetto M. On specimen design for size effect evaluation in ultrasonic gigacycle fatigue testing. *Fatigue Fract Eng Mater Struct.* 2014;37(5):570-579.

34. Tridello A, Paolino DS, Chiandussi G, Rossetto M. Effect of electroslag remelting on the VHCF response of an AISI H13 steel. *Fatigue Fract Eng Mater Struct.* 2017;40(11):1783-1794.

35. Haghshenas M, Simsiriwong J. Very high cycle fatigue behavior of additively manufactured metals using ultrasonic fatigue testing: a critical assessment of potentials and challenges. *Mater Perform Charact.* 2023;12(2):12.

36. Avateffazeli M, Haghshenas M. Ultrasonic fatigue of laser beam powder bed fused metals: a state-of-the-art review. *Eng Fail Anal.* 2022;134:106015.

37. Tridello A, Boursier Niutta C, Rossetto M, Berto F, Paolino DS. Statistical models for estimating the fatigue life, the stress–life relation, and the P-S–N curves of metallic materials in very high cycle fatigue: a review. *Fatigue Fract Eng Mater Struct.* 2022;45(2):332-370.

38. Yang P, Rodriguez MA, Deibler LA, et al. Effect of thermal annealing on microstructure evolution and mechanical behavior of an additive manufactured AlSi10Mg part. *J Mater Res.* 2018;33(12):1701-1712.

39. Lorenzino P, Navarro A. Grain size effects on notch sensitivity. *Int J Fatigue.* 2015;70:205-215.

40. Murakami Y. *Metal Fatigue: Effects of Small Defects and Nonmetallic Inclusions.* Elsevier; 2002.

41. Colombo C, Tridello A, Pagnoncelli AP, et al. Efficient experimental methods for rapid fatigue life estimation of additive manufactured elements. *Int J Fatigue.* 2023;167:107345.

42. Larrosa NO, Wang W, Read N, et al. Linking microstructure and processing defects to mechanical properties of selectively laser melted AlSi10Mg alloy. *Theor Appl Fract Mech.* 2018;98:123-133.

43. Wu Z, Wu S, Bao J, et al. The effect of defect population on the anisotropic fatigue resistance of AlSi10Mg alloy fabricated by laser powder bed fusion. *Int J Fatigue.* 2021;151:106317.

44. Tridello A, Fiocchi J, Biffi CA, et al. Effect of microstructure, residual stresses and building orientation on the fatigue response up to 109 cycles of an SLM AlSi10Mg alloy. *Int J Fatigue.* 2020;137:105659.

45. Du L, Qian G, Zheng L, Hong Y. Influence of processing parameters of selective laser melting on high-cycle and very-high-cycle fatigue behaviour of Ti-6Al-4V. *Fatigue Fract Eng Mater Struct.* 2021;44(1):240-256.

46. Masuo H, Tanaka Y, Morokoshi S, et al. Influence of defects, surface roughness and HIP on the fatigue strength of Ti-6Al-4V manufactured by additive manufacturing. *Int J Fatigue.* 2018;117:163-179.

47. Tridello A, Boursier Niutta C, Berto F, Qian G, Paolino DS. Fatigue failures from defects in additive manufactured components: a statistical methodology for the analysis of the experimental results. *Fatigue Fract Eng Mater Struct.* 2021;44(7):1944-1960.

48. Collins J. In: Wil, ed. *Failure of Materials in Mechanical Design—Analysis, Prediction, and Prevention.* Wiley; 2021.